

# Weakly-supervised Cross-view 3D Human Pose Estimation

Guoliang Hua\*, Wenhao Li\*, Qian Zhang, Runwei Ding and Hong Liu

Key Laboratory of Machine Perception, Shenzhen Graduate School, Peking University

{glhua, wenhaoli, qian.zhang, dingrunwei, hongliu}@pku.edu.cn

## Abstract

Although monocular 3D human pose estimation methods have made significant progress, it's far from being solved due to the inherent depth ambiguity. Instead, exploiting multi-view information is a practical way to achieve absolute 3D human pose estimation. In this paper, we propose a simple yet effective pipeline for weakly-supervised cross-view 3D human pose estimation. By only using two camera views, our method can achieve state-of-the-art performance in a weakly-supervised manner, requiring no 3D ground truth but only 2D annotations. Specifically, our method contains two steps: triangulation and refinement. First, given the 2D keypoints that can be obtained through any classic 2D detection methods, triangulation is performed across two views to lift the 2D keypoints into coarse 3D poses. Then, a novel cross-view U-shaped graph convolutional network (CV-UGCN), which can explore the spatial configurations and cross-view correlations, is designed to refine the coarse 3D poses. In particular, the refinement progress is achieved through weakly-supervised learning, in which geometric and structure-aware consistency checks are performed. We evaluate our method on the standard benchmark dataset, Human3.6M. The Mean Per Joint Position Error on the benchmark dataset is 27.4 mm, which outperforms the state-of-the-arts remarkably (27.4 mm vs 30.2 mm).

## 1 Introduction

3D human pose estimation aims to produce a 3-dimensional figure that describes the spatial position of the depicted person. This task has drawn tremendous attention in the past decades [Li and Chan, 2014; Chen and Ramanan, 2017; Zhou *et al.*, 2017], playing a significant role in many applications such as action recognition, virtual and augmented reality, human-robot interaction, etc. Many recent works [Martinez *et al.*, 2017; Xu *et al.*, 2020; Fabbri *et al.*, 2020] focus on estimating 3D human poses from monocular inputs, either

images or 2D keypoints. However, it is ill-posed due to the inherent depth ambiguity, since multiple 3D poses can map to the same 2D keypoints. As a result, most monocular methods only estimate the relative positions to the root joint and fail to estimate the absolute 3D poses, which greatly limits practical applications. Instead, exploiting multi-view information is arguably the best way to achieve absolute 3D pose estimation [Pavlakos *et al.*, 2017b].

Multi-view human pose estimation methods benefit from the complementary information from different camera views, e.g. multi-view geometric constraints to resolve the depth ambiguity, different views of the depicted person to deal with the occlusion problem. Many existing multi-view based methods [Isakov *et al.*, 2019; Qiu *et al.*, 2019; Kocabas *et al.*, 2019] follow a pipeline that first takes multi-view images as input to predict 2D detection heatmaps and then projects them to 3D poses through volumetric convolutional networks or Pictorial Structure Model (PSM) [Pavlakos *et al.*, 2017b; Chen and Yuille, 2014], as shown in Figure 1(a). However, using the convolutional neural network to perform 2D-3D lifting requires quantities of labeled 3D data as supervision, which is difficult and costly to collect. PSM discretizes the space around the root joint by an  $N \times N \times N$  grid and assigns each joint to one of the  $N^3$  bins (hypotheses), therefore requiring no 3D ground truth. However, the 2D-3D lifting accuracy of PSM based method is subject to the number of grids, and the computation complexity is of the order of  $O(N^6)$  which is computationally expensive.

To release the requirement of large quantities of 3D ground truth and take the computation complexity into consideration, a simple yet effective pipeline (see Figure 1(b)) is proposed in this paper for cross-view 3D human pose estimation. Different from other methods, our method estimates 3D human poses from coarse to fine and contains two steps: triangulation and refinement. Considering the increasing number of camera views will bring more computation and reduce the flexibility of application in the wild, we only use two camera views for training and inference. In the first step, we perform the triangulation between two camera views to lift 2D poses that can be obtained through any classic 2D keypoint detection methods to the 3D space. However, the triangulated 3D poses are noisy and unreliable due to the errors of 2D keypoint detection and camera parameters calibration, thus requiring further refinement.

\*Equal contribution.

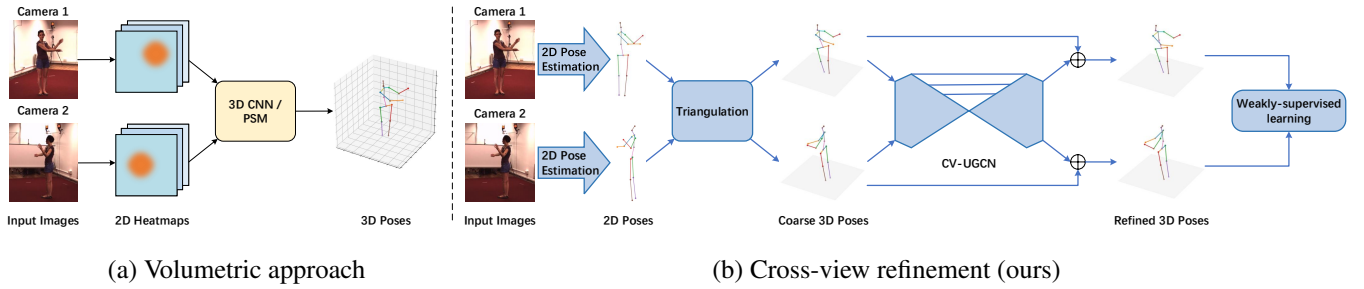


Figure 1: (a) Most state-of-the-arts use multi-view images as input and follow a pipeline that estimates 2D heatmaps and then directly recovers 3D poses through volumetric convolutional neural networks or Pictorial Structure Model (PSM). (b) We consider the 2D-3D lifting pipeline in a coarse-to-fine manner, which first obtains coarse 3D poses through triangulation from cross-view 2D joint detections and then refines the pose with a refinement model in a weakly-supervised manner.

In the refinement progress, a lightweight cross-view U-shaped graph convolutional network (CV-UGCN) is designed to refine the coarse 3D poses. As far as we know, it’s the first time that GCN is utilized to integrate cross-view information for 3D human pose estimation. By taking the cross-view coarse 3D poses as input, CV-UGCN is able to exploit spatial configurations and cross-view correlations to refine the poses to be more rational. Meanwhile, CV-UGCN is trained in a weakly-supervised manner, requiring no 3D ground truth but only 2D annotations. Specifically, by making full use of the cross-view geometric constraints, geometric and structure-aware consistency checks are introduced as the learning objective to train the network end-to-end.

We summarize our contributions as follows:

- A simple yet effective pipeline is proposed for cross-view 3D human pose estimation, which estimates the 3D human poses from coarse to fine by using the triangulation and the refinement model.
- A cross-view U-shaped graph convolutional network (CV-UGCN), which can take advantage of spatial configurations and cross-view correlations, is proposed as the refinement model.
- A weakly-supervised learning objective containing geometric and structure-aware consistency checks is introduced, therefore releasing from the requirement of large quantities of 3D ground truth for training.

Extensive experiments have been conducted on the benchmark dataset, Human3.6M, to verify the effectiveness of our method. The Mean Per Joint Position Error (MPJPE) on the benchmark dataset is 27.4 mm, which outperforms the state-of-the-arts remarkably (27.4 mm vs 30.2 mm).

## 2 Related Work

**Single-view 3D pose estimation.** Current promising solutions for monocular 3D pose estimation can be divided into two categories. Methods of the first category directly regress the 3D poses from monocular images. [Pavlakos *et al.*, 2017a] introduced a volumetric representation for 3D human poses, while required a sophisticated deep network architecture that is impractical in application. In the second category, these works first estimate 2D keypoints and then lift 2D poses

to the 3D space (2D-3D lifting). [Martinez *et al.*, 2017] predicted 3D poses via an effective fully-connected residual network and showed low error rates when using 2D ground truth as input. [Cai *et al.*, 2019] presented a local-to-global GCN to exploit spatial-temporal relationships to estimate 3D poses from a sequence of skeletons. Meanwhile, they introduced a pose refinement step to further improve the estimation accuracy. However, they only utilized the 2D detections to constrain the depth-normalized poses, while ignored the refinement for depth values. Different from [Cai *et al.*, 2019], we perform both 3D transformation and 2D reprojection consistency checks in our refinement model, so that the refinement is more sufficient.

**Multi-view 3D pose estimation.** In order to estimate the absolute 3D poses, recent works seek to utilize information from multiple synchronized cameras to solve the problem of depth ambiguity. Most multi-view based approaches use 3D volumes to aggregate 2D heatmap predictions. [Qiu *et al.*, 2019] presented a cross-view fusion scheme to jointly estimate 2D heatmaps of multiple views and then used a recursive Pictorial Structure Model to estimate the absolute 3D poses. [Iskakov *et al.*, 2019] proposed a learnable triangulation method to regress 3D poses from multiple views. However, volumetric approaches are computationally demanding. To recover 3D poses from multi-view images without using compute-intensive volumetric grids, [Remelli *et al.*, 2020] exploited 3D geometry to fuse input images into a unified latent representation of poses. Different from these methods that embedded the improved 2D detector into their model to obtain more accurate 2D poses to further improve the 3D pose estimation, our method focuses on the task of 2D-3D lifting and can be easily integrated with any 2D detectors to achieve 3D pose estimation with a lightweight refinement model.

**Weakly/self-supervised methods.** Because 3D human pose datasets are limited and collecting 3D human pose annotations is costly, researchers have resorted to weakly or self-supervised approaches. [Zhou *et al.*, 2017] proposed a weakly-supervised transfer learning method, which is effective in the absence of depth labels. To tackle the overfitting problem, [Wandt and Rosenhahn, 2019] proposed a weakly-supervised reprojection network (RepNet) by using an adversarial training approach, which generalized well to unknown

data. Moreover, in [Kundu *et al.*, 2020], a self-supervised learning method was proposed to estimate 3D poses from unlabeled video frames that disentangled the inherent factors of variations via part guided human image synthesis. Compared with previous methods, our method has the advantage of decomposing the challenging 3D human pose estimation task into two steps and making full use of geometric and structure-aware consistency checks for weakly-supervised learning.

### 3 Cross-view 3D Human Pose Estimation

Figure 1 (b) depicts our pipeline for weakly-supervised cross-view 3D human pose estimation. Given the estimated 2D poses  $x_i \in \mathbb{R}^{J \times 2}$  from two different views, we aim at recovering their absolute 3D poses  $X_i \in \mathbb{R}^{J \times 3}$ , where  $i$  is the index of the camera views, and  $J$  is the number of joints. In particular, we first reconstruct coarse 3D poses through the triangulation. Then, a cross-view U-shaped graph convolutional network (CV-UGCN) is proposed to refine the coarse triangulated 3D poses to obtain more precise estimations.

#### 3.1 Triangulation

Assuming two cameras are synchronized and calibrated, triangulation can be performed between two camera views to lift 2D poses into the 3D space. Given the 2D joint locations  $x_1, x_2$  of two camera views, which can be obtained through classic 2D keypoint detection methods, the triangulation is solved through

$$\begin{bmatrix} x_1^j \times I \\ x_2^j \times T_{c_2, c_1} \end{bmatrix} \tilde{X}_1^j = 0, \quad (1)$$

where  $x_1^j, x_2^j$  are the 2D coordinates of  $j$ -th joint,  $I$  is the identity matrix,  $T_{c_2, c_1}$  is the transformation matrix between the camera  $c_2$  and  $c_1$ . By solving Eq. (1) through Singular Value Decomposition (SVD), the 3D pose  $\tilde{X}_1$  of the camera  $c_1$  can be obtained. Similarly, we can obtain the 3D pose  $\tilde{X}_2$  of the camera  $c_2$ .

Although triangulation is a straightforward way to achieve 2D-3D lifting, it is subject to the accuracy of the 2D joint detections and the precision of calibrated camera parameters. To solve this problem, Qiu *et al.* proposed a more robust Recursive Pictorial Structure Model (RPSM) to replace the triangulation [Qiu *et al.*, 2019]. Different from them, we propose to optimize the coarse triangulated 3D poses through a weakly-supervised learning refinement model, which is lightweight and requires no 3D annotations for training.

#### 3.2 Cross-view Refinement Model

In order to refine the coarse triangulated 3D poses, a cross-view refinement model is proposed. Specifically, we design a cross-view U-shaped graph convolutional network, named CV-UGCN, which can make full use of the spatial configurations and cross-view correlations for refinement. As specified in Figure 3, the CV-UGCN takes the cross-view coarse 3D poses as input and outputs the residual shift added to the coarse 3D poses to obtain the refined 3D poses.

**Graph modeling.** Here, we first give the definition of the graph model of CV-UGCN. The cross-view skeletons are organized as an undirected graph in the spatial and camera-view

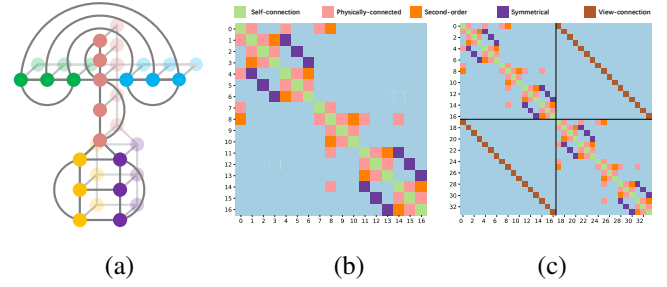


Figure 2: (a) The human skeleton graph in kinematic connections and cross-view connections. (b) The adjacency matrix of single-view GCN. (c) The adjacency matrix of multi-view GCN (2 views).

domains. The undirected graph  $\mathbb{G}$  contains a set of vertices  $\mathcal{V}$  and edges  $\mathcal{E}$ , where  $\mathcal{V} = \{v_{ij} \mid i = 1, \dots, V; j = 1, \dots, J\}$  corresponds to  $J$  joints of human body in  $V$  camera views. For single-view GCN (S-GCN) that processes data from a single view, the edge  $\mathcal{E}$  only consists of kinematic connections of spatial configurations. For multi-view GCN (M-GCN) that embeds additional cross-view correlations into the graph model, the edge  $\mathcal{E}$  consists of two parts: kinematic connections and cross-view connections.

**Graph convolution.** As presented in Figure 2, the defined undirected graph is represented in an adjacency matrix  $A \in \mathbb{R}^{N \times N}$ , where  $N = VJ$  ( $N = J$  for S-GCN). In detail, the graph nodes are classified as the neighboring nodes according to their semantic meanings in the human body structure, and five kernels are used for different neighboring nodes: 1) self-connection nodes; 2) physical-connection nodes; 3) second-order connection nodes; 4) symmetrical nodes; 5) view-connection nodes. Note that S-GCN only processes single-view data, thus having no view-connection nodes.

Given the input signal  $H \in \mathbb{R}^{N \times C}$  with  $C$  channels, we update the graph convolution operation in [Kipf and Welling, 2016] by dismantling adjacent matrix into  $k$  sub-matrices to:

$$Z = \sum_k \tilde{D}_k^{-\frac{1}{2}} \tilde{A}_k \tilde{D}_k^{-\frac{1}{2}} H W_k, \quad (2)$$

where  $Z \in \mathbb{R}^{N \times F}$  is the convolved signal matrix,  $W_k \in \mathbb{R}^{C \times F}$ ,  $\tilde{A}_k \in \mathbb{R}^{N \times N}$  are a learnable filter matrix and the normalized adjacency matrix for the  $k$ -th type of neighboring nodes respectively, and  $\tilde{D}_k^{ii} = \sum_j \tilde{A}_k^{ij}$ .

**Network structure.** As specified in Figure 3, S-GCN and M-GCN units are basic blocks to build the CV-UGCN. The cross-view coarse 3D poses are first fed into S-GCN units independently to capture the spatial configurations. In this way, the structure-aware information can be fully explored in each view. Then, we concatenate them into a shared latent space via the fusion layer to fuse the features of two views for cross-view information interactions, so that the cross views can compensate for each other.

Furthermore, inspired by the success of U-shaped architecture [Ronneberger *et al.*, 2015], we build an UGCN architecture by exploiting the M-GCN unit, graph pooling, and

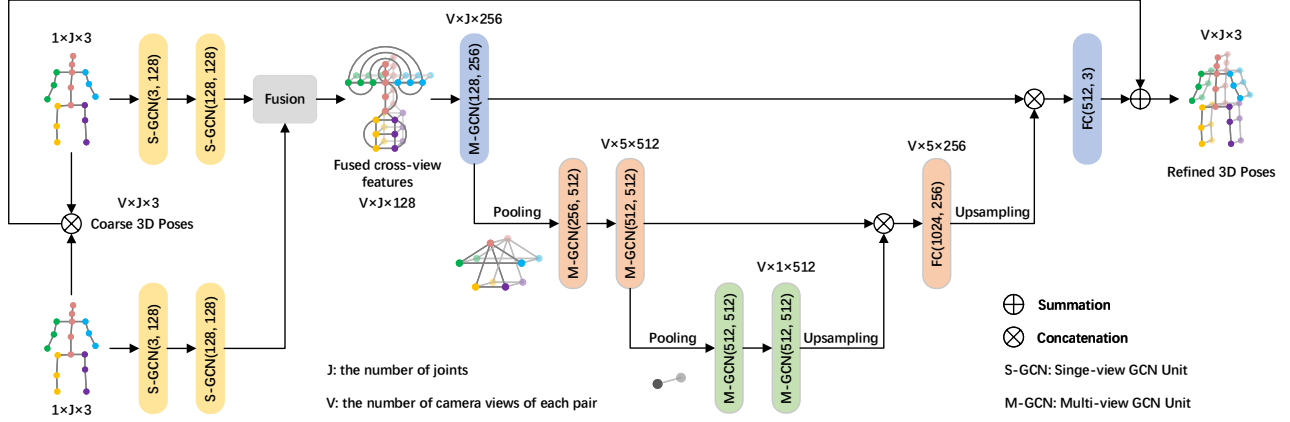


Figure 3: A schematic of CV-UGCN. S-GCN units are first utilized to preprocess the coarse 3D poses of each view to capture spatial configurations independently. Then, the fused cross-view features are fed into the U-shaped architecture, where M-GCN units are utilized to explore additional cross-view correlations.

graph upsampling operations, as shown in Figure 3. As a result, the features in the cross-view spatial graph model can be integrated in a multi-scale manner, assisting to obtain more accurate pose refinement.

Thanks to the spatial configurations and cross-view correlations that are fully explored in our CV-UGCN, the precise residual shift is predicted for 3D pose refinement. By adding the residual shift to the triangulated 3D coarse poses  $\tilde{X}$ , we can obtain the accurate refined poses  $X = \mathcal{G}(\tilde{X}) + \tilde{X}$ , where  $\mathcal{G}$  denotes the refinement function of CV-UGCN.

## 4 Weakly-supervised Learning Approach

To relieve the requirement of 3D ground truth for supervised learning, a weakly-supervised learning objective is designed and only needs 2D annotations that are much easier to gather. Geometric and structure-aware consistency checks are performed in both single-view and cross-view manners.

### 4.1 Single-view Optimization

We first impose the geometric and structure-aware consistency checks for each view to perform single-view optimization, by considering the 2D reprojection consistency and left-right symmetry prior.

**2D reprojection loss.** After the coarse 3D pose is refined by CV-UGCN, we reproject the refined 3D pose into the 2D joint location through  $x = Z^{-1}KX$ , where  $X$  is the refined 3D pose,  $x$  is the reprojected 2D pose,  $K$  is the camera intrinsic parameter, and  $Z$  is the depth value. Then, the 2D reprojection loss is introduced to penalize the error between  $x$  and 2D ground truth  $y$ :

$$L_r = \sum_{i=1}^V \sum_{j=1}^J \|y_i^j - x_i^j\|_2, \quad (3)$$

where  $i, j$  index the camera views and joints respectively.

**Symmetry loss.** Noticing that the structure of human body is left-right symmetrical, a symmetry loss is introduced to constrain the bone length of the left part and the right part

to be the same. It is effective to alleviate the depth ambiguity problem especially when the occlusion happens [Dabral *et al.*, 2018]. The symmetry loss is defined as

$$L_s = \sum_{i=1}^V \sum_k \|B_i^k - B_i^{C(k)}\|_2, \quad (4)$$

where  $B_i^k = \|X_i^{k_1} - X_i^{k_2}\|$  is the estimated bone length for a left-side bone  $k$  of  $i$ -th camera view, and  $C(k)$  is the corresponding right-side bone,  $k_1$  and  $k_2$  are the joints of the  $k$ -th bone.

### 4.2 Cross-view Optimization

It's quite often that some joints are unseen or close with each other in one view, which brings significant challenges for single-view optimization. Therefore, we perform cross-view optimization to take advantage of cross-view consistency priors.

Given the refined 3D poses of two views,  $X_1, X_2$ , cross-view 3D transformation is performed to generate the poses of camera view  $c_1$  from  $c_2$  by  $X_{1 \leftarrow 2} = T_{c_1, c_2} \cdot X_2$ . Similarly, we can obtain the  $X_{2 \leftarrow 1}$  transformed from  $X_1$ .

**3D transformation consistency loss.** The transformed poses should keep consistency with the original 3D poses, thus we calculate the 3D transformation consistency loss as follows:

$$L_t = \sum_{i=1}^V \sum_{j=1}^J (\|X_1^j - X_{1 \leftarrow 2}^j\|_2 + \|X_2^j - X_{2 \leftarrow 1}^j\|_2). \quad (5)$$

**Bone direction consistency loss.** As each joint is always penalized independently, it is prone to fall into local optimum because of ignoring the graph structure of human body. Therefore, the bone direction consistency loss is designed to check the bone direction keeping consistency between the original poses and the transformed poses. We first compute the bone vector to represent the bone direction,  $\mathbf{b}^k = \vec{ok_1} - \vec{ok_2} = X^{k_1} - X^{k_2}$ . Then, the bone direction



Protocol #1	V	GT	Dir.	Disc	Eat	Greet	Phone	Photo	Pose	Purch.	Sit	SitD.	Smoke	Wait	WalkD.	Walk	WalkT.	Avg.
Martinez et al. (ICCV'17)	1	✓	51.8	56.2	58.1	59.0	69.5	78.4	55.2	58.1	74.0	94.6	62.3	59.1	65.1	49.5	52.4	62.9
Cai et al. (ICCV'19)	1	✓	44.6	47.4	45.6	48.8	50.8	59.0	47.2	43.9	57.9	61.9	49.7	46.6	51.3	37.1	39.4	48.8
Pavlo et al. (CVPR'19)	1	✓	45.2	46.7	43.3	45.6	48.1	55.1	44.6	44.3	57.3	65.8	47.1	44.0	49.0	32.8	33.9	46.8
Wang et al. (ECCV'20)	1	✓	38.2	41.0	45.9	39.7	41.4	51.4	41.6	41.4	52.0	57.4	41.8	44.4	41.6	33.1	30.0	42.6
Pavlakos et al. (CVPR'17)	4	✓	41.2	49.2	42.8	43.4	55.6	46.9	40.3	63.7	97.6	119.0	52.1	42.7	51.9	41.8	39.4	56.9
Tome et al. (3DV'18)	4		43.3	49.6	42.0	48.8	51.1	64.3	40.3	43.3	66.0	95.2	50.2	52.2	51.1	43.9	45.3	52.8
Chen et al. (CVPR'19)	2		41.1	44.2	44.9	45.9	46.5	39.3	41.6	54.8	73.2	46.2	48.7	42.1	35.8	46.6	38.5	46.3
Qiu et al. (CVPR'19)	4		28.9	32.5	26.6	28.1	<b>28.3</b>	<b>29.3</b>	28.0	36.8	41.0	<b>30.5</b>	35.6	30.0	28.3	30.0	30.5	31.2
He et al. (CVPR'20)	4		29.0	30.6	27.4	26.4	31.0	31.8	26.4	28.7	34.2	42.6	32.4	29.3	27.0	29.3	25.9	30.4
Remelli et al. (CVPR'20)	4	✓	<u>27.3</u>	32.1	<b>25.0</b>	26.5	29.3	35.4	28.8	31.6	36.4	<u>31.7</u>	<u>31.2</u>	29.9	<b>26.9</b>	33.7	30.4	<u>30.2</u>
Ours	2		<b>25.6</b>	<b>27.7</b>	<u>25.3</u>	<b>24.5</b>	29.1	<u>29.5</u>	<b>23.5</b>	<b>25.7</b>	<b>31.2</b>	37.3	<b>28.9</b>	<b>24.9</b>	28.8	<b>24.6</b>	<b>24.8</b>	<b>27.4</b>

Table 1: Quantitative comparisons of Mean Per Joint Position Error (MPJPE) in millimeter on Human3.6M under protocol #1. V is the number of camera views for training and inference. GT means these methods using 3D ground truth to train the model. The best score is marked in bold, and the second best is underlined.

consistency loss is calculated as follows:

$$L_b = \sum_k (1 - \frac{\mathbf{b}_1^k \cdot \mathbf{b}_{1 \leftarrow 2}^k}{\|\mathbf{b}_1^k\| \|\mathbf{b}_{1 \leftarrow 2}^k\|}) + \sum_k (1 - \frac{\mathbf{b}_2^k \cdot \mathbf{b}_{2 \leftarrow 1}^k}{\|\mathbf{b}_2^k\| \|\mathbf{b}_{2 \leftarrow 1}^k\|}), \quad (6)$$

where  $k$  is the index of bone for human body,  $k_1$  and  $k_2$  are the joints of the  $k$ -th bone.

### 4.3 Learning Objective

By performing both the single-view optimization and cross-view optimization, we combine the introduced losses: a 2D reprojection loss  $L_r$ , a symmetry loss  $L_s$ , a 3D transform consistency loss  $L_t$ , and a bone direction consistency loss  $L_b$ , as the final weakly-supervised learning objective,

$$L = \lambda_r L_r + \lambda_s L_s + \lambda_t L_t + \lambda_b L_b, \quad (7)$$

where  $\lambda_r = 1$ ,  $\lambda_s = 1$ ,  $\lambda_t = 1$  and  $\lambda_b = 0.1$  are weighting factors.

## 5 Experiments

### 5.1 Datasets and Evaluation Metrics

We mainly evaluate our method on the standard benchmark dataset, Human3.6M [Ionescu *et al.*, 2013]. More experimental results (further analysis, experiments on other datasets, and applying our method to the real scene) can be seen in the supplementary.

**Human3.6M.** The Human3.6M dataset is the largest publicly available dataset for 3D human pose estimation, which consists of 3.6 million images captured from 4 synchronized 50 Hz cameras. Following the standard protocol in prior work [Chen *et al.*, 2019; Tome *et al.*, 2018], we use 5 subjects (S1, S5, S6, S7, S8) for training and 2 subjects (S9 and S11) for evaluation.

**Evaluation Metrics.** We report the Mean Per Joint Position Error (MPJPE) to measure the 3D pose estimation accuracy. MPJPE is the evaluation metric referred to as protocol #1 in many works [Fang *et al.*, 2018; Kocabas *et al.*, 2019], which calculates the average Euclidean distance between the ground truth and predictions.

### 5.2 Implementation Details

In this work, all experiments are conducted on the PyTorch framework with one GeForce GTX 2080 Ti GPU. The network is trained using Adam optimizer with a mini-batch size

Method	MPJPE (mm)	$\Delta$
w/o refinement	36.0	8.6
Ours w/o spatial configuration	31.5	4.1
Ours w/o cross-view correlation	29.3	1.9
Ours w/o fusion	28.2	0.8
Ours (CV-UGCN)	27.4	-

Table 2: Ablation studies on each component of CV-UGCN. The evaluation is performed on Human3.6M with the MPJPE metric under the protocol #1.

Method	MPJPE (mm)	$\Delta$
$L_r$	28.3	0.9
$L_r + L_s$	28.2	0.8
$L_r + L_t$	28.1	0.7
$L_r + L_b$	27.9	0.5
$L_r + L_s + L_b$	27.8	0.4
$L_r + L_s + L_b + L_t$	27.4	-

Table 3: Ablation studies on each term of the weakly-supervised losses.

of 256 for Human3.6M. An initial learning rate of 0.001 is used and decreases by 0.9 whenever the training loss does not decrease for every 10 epochs.

Different from other multi-view methods that use all the camera views provided by the dataset, we only utilize two camera views for training and inference due to the consideration of computation complexity and implementation flexibility. For Human3.6M, adjacent camera pairs (c1 and c2, c1 and c3, c2 and c4, c3 and c4) are used for training and testing.

The 2D poses can be obtained by performing any classic 2D detection methods or directly using the 2D ground truth. Following [Pavlo *et al.*, 2019], we utilize the cascaded pyramid network (CPN) [Chen *et al.*, 2018] to obtain 2D poses of Human3.6M dataset for a fair comparison.

### 5.3 Comparison to the State-of-the-arts

As shown in Table 5, we report the MPJPE results on Human3.6M of various methods, monocular-based or multi-view based, using 3D ground truth or not, for a complete comparison. Compared with them, our method makes a further

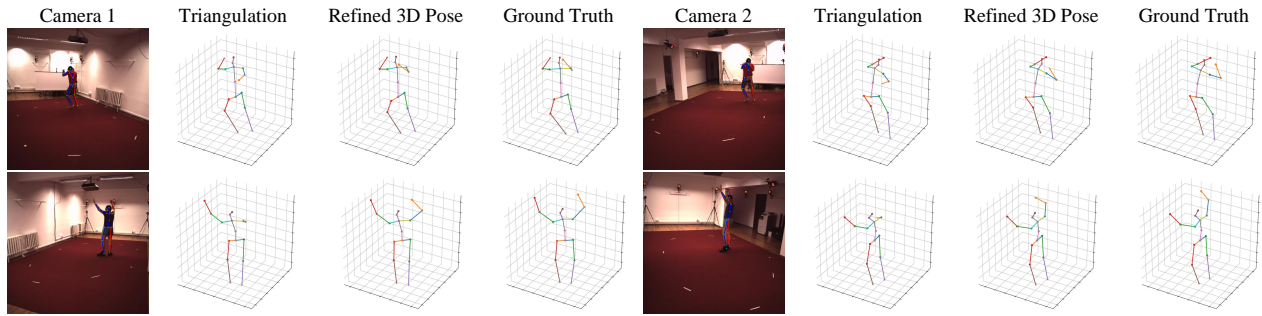


Figure 4: Qualitative results of our approach. The results of triangulation are noisy and unreliable, while our model is able to produce realistic and structurally plausible 3D poses.

improvement and gains a new state-of-the-art performance of 27.4 mm, benefiting from our effective refinement model and the novel weakly-supervised learning objective.

Figure 4 shows some qualitative results on the Human3.6M. It can be seen that the triangulated results are noisy and unreliable due to the 2D detection and camera parameters calibration errors, while the refined 3D poses are realistic and structurally plausible. This demonstrates the effectiveness of our refinement model to refine the coarse triangulated 3D poses.

#### 5.4 Ablation Studies

**Effect of CV-UGCN.** An ablation study is performed by changing various components of CV-UGCN to show the contribution of each component of our refinement model, as presented in Table 2. Without exploiting the refinement model, the triangulated results are noisy with the MPJPE of 36.0 mm. CV-UGCN can refine the coarse 3D poses and bring significant improvement (8.6 mm). When removing the spatial configuration or cross-view correlation from the adjacency matrix of CV-UGCN, the performance decreases. It verifies the importance of considering both the spatial configuration and cross-view correlation in the graph model. Meanwhile, without first using S-GCN to preprocess the coarse poses of each view and then fusing the features for M-GCN, the result (ours w/o fusion) also decreases. It is because that the triangulated poses are too noisy to conduct cross-view information interaction well in the early stage.

**Effect of weakly-supervised losses.** In Table 3, we investigate the effect of each component of our weakly-supervised learning objective. When only using the reprojection loss  $L_r$ , the MPJPE is 28.3 mm. If  $L_r$  works with an additional loss (symmetry loss  $L_s$ , 3D transform consistency loss  $L_t$  or bone length consistency loss  $L_b$ ), the performance is improved. At last, as more components are used, the results are better. This is attributed to the joint geometric and structure-aware consistency checks that are performed in both single-view and cross-view optimization manners.

#### 5.5 Model Size and Inference Time

We report the model size and inference time to show the efficiency of our methods. Table 4 exhibits the comparison of the model size and performance with the recent methods [Qiu *et al.*, 2019; Isakov *et al.*, 2019; Remelli *et al.*, 2020]. Because

Method	$V$	GT	Model Size	MPJPE (mm)
Qiu <i>et al.</i> (CVPR'19)	4		2.1 GB	31.2
Isakov <i>et al.</i> (ICCV'19)	4	✓	643 MB	20.8
Remelli <i>et al.</i> (CVPR'20)	4	✓	251 MB	30.2
CPN + Ours	2		47 MB	27.4
2D-GT + Ours	2		20 MB	1.1

Table 4: Model size and performance comparison. GT means these methods using 3D ground truth to train the model.  $V$  is the number of camera views for training and inference. 2D-GT + Ours represents that using 2D ground truth as input.

the comparison methods embedded the 2D detector into their model, we add the model size of CPN [Chen *et al.*, 2018] to ours for a fair comparison. It can be seen that our method can achieve impressive performance with a lightweight model.

On a machine equipped with one GeForce 2080 Ti GPU, the 2D detector CPN requires about 0.02 s to perform the 2D detection, while our pipeline needs about another 0.01 s to estimate the 3D poses. Consequently, estimating 3D poses from images of two camera views, our method could yield a real-time performance ( $\sim 33$  fps). Note that if a better and faster 2D detector is used with our method, the performance and speed can have a further improvement.

## 6 Conclusion

In this paper, a simple yet effective pipeline is proposed for cross-view 3D human pose estimation. Specifically, performing in a coarse-to-fine manner, we first exploit triangulation to lift the 2D detections to coarse 3D poses, and then utilize the refinement model to obtain the precise results. In particular, a novel cross-view U-shaped graph convolutional network (CV-UGCN) is designed as the refinement model, which can take advantage of spatial configurations and cross-view correlations to accurately refine the coarse 3D poses. Moreover, to release from the requirement of quantities of 3D ground truth as supervision, we introduce a weakly-supervised learning objective by exploiting geometric and structure-aware consistency checks in single-view and cross-view optimizations. Extensive experiments have been done on the benchmark dataset. The results show that our method not only achieves state-of-the-art performance but also is lightweight and could run in real-time.

## References

- [Cai *et al.*, 2019] Yujun Cai, Lihao Ge, Jun Liu, Jianfei Cai, Tat-Jen Cham, Junsong Yuan, and Nadia Magnenat Thalmann. Exploiting spatial-temporal relationships for 3d pose estimation via graph convolutional networks. In *Proceedings of the IEEE International Conference on Computer Vision (ICCV)*, pages 2272–2281, 2019.
- [Chen and Ramanan, 2017] Ching-Hang Chen and Deva Ramanan. 3d human pose estimation= 2d pose estimation+ matching. In *Proceedings of the IEEE Conference on Computer Vision and Pattern Recognition (CVPR)*, pages 7035–7043, 2017.
- [Chen and Yuille, 2014] Xianjie Chen and Alan L Yuille. Articulated pose estimation by a graphical model with image dependent pairwise relations. In *Advances in Neural Information Processing Systems (NeurIPS)*, pages 1736–1744, 2014.
- [Chen *et al.*, 2018] Yilun Chen, Zhicheng Wang, Yuxiang Peng, Zhiqiang Zhang, Gang Yu, and Jian Sun. Cascaded pyramid network for multi-person pose estimation. In *Proceedings of the IEEE Conference on Computer Vision and Pattern Recognition (CVPR)*, pages 7103–7112, 2018.
- [Chen *et al.*, 2019] Xipeng Chen, Kwan-Yee Lin, Wentao Liu, Chen Qian, and Liang Lin. Weakly-supervised discovery of geometry-aware representation for 3d human pose estimation. In *Proceedings of the IEEE Conference on Computer Vision and Pattern Recognition (CVPR)*, pages 10895–10904, 2019.
- [Dabral *et al.*, 2018] Rishabh Dabral, Anurag Mundhada, Uday Kusupati, Safeer Afaq, Abhishek Sharma, and Arjun Jain. Learning 3d human pose from structure and motion. In *Proceedings of the European Conference on Computer Vision (ECCV)*, pages 668–683, 2018.
- [Fabbri *et al.*, 2020] Matteo Fabbri, Fabio Lanzi, Simone Calderara, Stefano Alletto, and Rita Cucchiara. Compressed volumetric heatmaps for multi-person 3d pose estimation. In *Proceedings of the IEEE Conference on Computer Vision and Pattern Recognition (CVPR)*, pages 7204–7213, 2020.
- [Fang *et al.*, 2018] Hao-Shu Fang, Yuanlu Xu, Wenguan Wang, Xiaobai Liu, and Song-Chun Zhu. Learning pose grammar to encode human body configuration for 3d pose estimation. In *Thirty-Second AAAI Conference on Artificial Intelligence*, 2018.
- [He *et al.*, 2020] Yihui He, Rui Yan, Katerina Fragkiadaki, and Shoubo Yu. Epipolar transformers. In *Proceedings of the IEEE Conference on Computer Vision and Pattern Recognition (CVPR)*, pages 7779–7788, 2020.
- [Ionescu *et al.*, 2013] Catalin Ionescu, Dragos Papava, Vlad Olaru, and Cristian Sminchisescu. Human3.6m: Large scale datasets and predictive methods for 3d human sensing in natural environments. *IEEE Transactions on Pattern Analysis and Machine Intelligence*, 36(7):1325–1339, 2013.
- [Iqbal *et al.*, 2020] Umar Iqbal, Pavlo Molchanov, and Jan Kautz. Weakly-supervised 3d human pose learning via multi-view images in the wild. In *Proceedings of the IEEE Conference on Computer Vision and Pattern Recognition (CVPR)*, pages 5243–5252, 2020.
- [Iskakov *et al.*, 2019] Karim Iskakov, Egor Burkov, Victor Lempitsky, and Yury Malkov. Learnable triangulation of human pose. In *Proceedings of the IEEE International Conference on Computer Vision (ICCV)*, pages 7718–7727, 2019.
- [Kipf and Welling, 2016] Thomas N Kipf and Max Welling. Semi-supervised classification with graph convolutional networks. *arXiv preprint arXiv:1609.02907*, 2016.
- [Kocabas *et al.*, 2019] Muhammed Kocabas, Salih Karagoz, and Emre Akbas. Self-supervised learning of 3d human pose using multi-view geometry. In *Proceedings of the IEEE Conference on Computer Vision and Pattern Recognition (CVPR)*, pages 1077–1086, 2019.
- [Kundu *et al.*, 2020] Jogendra Nath Kundu, Siddharth Seth, Varun Jampani, Mugalodi Rakesh, R Venkatesh Babu, and Anirban Chakraborty. Self-supervised 3d human pose estimation via part guided novel image synthesis. In *Proceedings of the IEEE Conference on Computer Vision and Pattern Recognition (CVPR)*, pages 6152–6162, 2020.
- [Lee *et al.*, 2018] Kyoungoh Lee, Inwoong Lee, and Sanghoon Lee. Propagating lstm: 3d pose estimation based on joint interdependency. In *Proceedings of the European Conference on Computer Vision (ECCV)*, pages 119–135, 2018.
- [Li and Chan, 2014] Sijin Li and Antoni B Chan. 3d human pose estimation from monocular images with deep convolutional neural network. In *Asian Conference on Computer Vision (ACCV)*, pages 332–347, 2014.
- [Martinez *et al.*, 2017] Julieta Martinez, Rayat Hossain, Javier Romero, and James J Little. A simple yet effective baseline for 3d human pose estimation. In *Proceedings of the IEEE International Conference on Computer Vision (ICCV)*, pages 2640–2649, 2017.
- [Newell *et al.*, 2016] Alejandro Newell, Kaiyu Yang, and Jia Deng. Stacked hourglass networks for human pose estimation. In *European conference on computer vision (ECCV)*, pages 483–499, 2016.
- [Pavlakos *et al.*, 2017a] Georgios Pavlakos, Xiaowei Zhou, Konstantinos G Derpanis, and Kostas Daniilidis. Coarse-to-fine volumetric prediction for single-image 3d human pose. In *Proceedings of the IEEE Conference on Computer Vision and Pattern Recognition (CVPR)*, pages 7025–7034, 2017.
- [Pavlakos *et al.*, 2017b] Georgios Pavlakos, Xiaowei Zhou, Konstantinos G Derpanis, and Kostas Daniilidis. Harvesting multiple views for marker-less 3d human pose annotations. In *Proceedings of the IEEE Conference on Computer Vision and Pattern Recognition (CVPR)*, pages 6988–6997, 2017.
- [Pavlo *et al.*, 2019] Dario Pavlo, Christoph Feichtenhofer, David Grangier, and Michael Auli. 3d human pose estimation in video with temporal convolutions and semi-supervised training. In *Proceedings of the IEEE Conference on Computer Vision and Pattern Recognition (CVPR)*, pages 7753–7762, 2019.
- [Qiu *et al.*, 2019] Haibo Qiu, Chunyu Wang, Jingdong Wang, Naiyan Wang, and Wenjun Zeng. Cross view fusion for 3d human pose estimation. In *Proceedings of the IEEE International Conference on Computer Vision (ICCV)*, pages 4342–4351, 2019.
- [Remelli *et al.*, 2020] Edoardo Remelli, Shangchen Han, Sina Honari, Pascal Fua, and Robert Wang. Lightweight multi-view 3d pose estimation through camera-disentangled representation. In *Proceedings of the IEEE Conference on Computer Vision and Pattern Recognition (CVPR)*, pages 6040–6049, 2020.
- [Ronneberger *et al.*, 2015] Olaf Ronneberger, Philipp Fischer, and Thomas Brox. U-net: Convolutional networks for biomedical image segmentation. In *International Conference on Medical Image Computing and Computer-assisted Intervention*, pages 234–241, 2015.
- [Tome *et al.*, 2017] Denis Tome, Chris Russell, and Lourdes Agapito. Lifting from the deep: Convolutional 3d pose estimation from a single image. In *Proceedings of the IEEE Conference on Computer Vision and Pattern Recognition (CVPR)*, pages 2500–2509, 2017.

- [Tome *et al.*, 2018] Denis Tome, Matteo Toso, Lourdes Agapito, and Chris Russell. Rethinking pose in 3d: Multi-stage refinement and recovery for markerless motion capture. In *2018 International Conference on 3D Vision (3DV)*, pages 474–483, 2018.
- [Trumble *et al.*, 2017] Matthew Trumble, Andrew Gilbert, Charles Malleson, Adrian Hilton, and John Collomosse. Total capture: 3d human pose estimation fusing video and inertial sensors. In *Proceedings of the British Machine Vision Conference (BMVC)*, pages 1–13, 2017.
- [Wandt and Rosenhahn, 2019] Bastian Wandt and Bodo Rosenhahn. Repnet: Weakly supervised training of an adversarial re-projection network for 3d human pose estimation. In *Proceedings of the IEEE Conference on Computer Vision and Pattern Recognition (CVPR)*, pages 7782–7791, 2019.
- [Wang *et al.*, 2019] Chaoyang Wang, Chen Kong, and Simon Lucey. Distill knowledge from nrsfm for weakly supervised 3d pose learning. In *Proceedings of the IEEE International Conference on Computer Vision (ICCV)*, pages 743–752, 2019.
- [Wang *et al.*, 2020] Jingbo Wang, Sijie Yan, Yuanjun Xiong, and Dahua Lin. Motion guided 3d pose estimation from videos. *arXiv preprint arXiv:2004.13985*, 2020.
- [Xu *et al.*, 2020] Jingwei Xu, Zhenbo Yu, Bingbing Ni, Jiancheng Yang, Xiaokang Yang, and Wenjun Zhang. Deep kinematics analysis for monocular 3d human pose estimation. In *Proceedings of the IEEE Conference on Computer Vision and Pattern Recognition (CVPR)*, pages 899–908, 2020.
- [Zhou *et al.*, 2017] Xingyi Zhou, Qixing Huang, Xiao Sun, Xi-angyang Xue, and Yichen Wei. Towards 3d human pose estimation in the wild: a weakly-supervised approach. In *Proceedings of the IEEE International Conference on Computer Vision (ICCV)*, pages 398–407, 2017.



# Supplemental Material: Weakly-supervised Cross-view 3D Human Pose Estimation

## Abstract

In this supplementary file, we first report more comparisons to the state-of-the-arts in Section 7. Then, the analysis of the impact of using different 2D detections as inputs is given in Section 8. We test the generalization ability of our refinement model to unseen cameras in Section 9. In Section 10, we evaluate the influence of different weighting factors for bone direction consistency loss. Besides, we evaluate the robustness of CV-UGCN on the HumanEva-I dataset in Section 11. More visualization results are provided in Section 12. Finally, we apply our method to the real scene to test the applicability in Section 13.

## 7 Comparison to the State-of-the-arts

Here, we report more comparison results on Human3.6M dataset. As shown in Table 1,  $V$  denotes the number of camera views that the method exploits, GT represents whether the method requires the 3D ground truth as supervision. In this way, methods are divided into monocular based or multi-view based, supervised or weakly/self-supervised for a complete comparison. It can be seen that our method can make a trade-off between the performance and the additional data requirement, which achieves state-of-the-art performance by only using 2 camera views and requiring no 3D annotations to train the model.

## 8 The Impact of Different 2D Detections

For the 2D-3D lifting task, the accuracy of the 2D detections directly influences the results of 3D pose estimation [Martinez *et al.*, 2017]. We utilize Stack Hourglass (SH) [Newell *et al.*, 2016], Detectron [Pavlo *et al.*, 2019], CPN [Chen *et al.*, 2018], and 2D ground truth (GT) with different levels of additive Gaussian noises to explore the impact of different 2D detections. Figure 5 shows the relationship between the MPJPE of 3D poses and two-norm errors of 2D detections. For both the triangulation and the refinement, the MPJPE of 3D poses increases linearly with the two-norm errors of 2D detections. However, it can be observed that our refinement model has a lower incremental rate than triangulation, verifying the effectiveness of our refinement model to refine the triangulated 3D poses.

## 9 Generalization to Unseen Cameras

To validate the feasibility of applying our model to unknown views, we train the model on some paired views and evaluate its performance on other unseen camera pairs. The results are presented in Table 6, where  $P_i$  denotes  $i$ -th paired views. It can be observed that CV-UGCN still can improve the triangulated results in some unseen camera views, which verifies the generalization capability of our method.

## 10 Hyperparameter Evaluations

Due to the bone direction consistency loss is calculated by measuring the cosine distance between two bone vectors which is different from other losses that calculate the RMSE, it's necessary to find a proper weighting factor for  $L_b$ . As shown in Figure 6, the best performance is achieved when  $\lambda_b$  equals to 0.1.

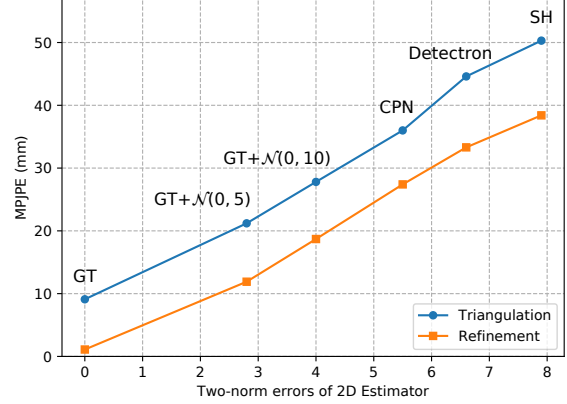


Figure 5: The impact of 2D detections. Experiments are performed on Human3.6M with the MPJPE metric under the protocol #1.  $\mathcal{N}(0, \sigma^2)$  represents the Gaussian noise with mean zero and standard deviation  $\sigma$ . GT denotes the 2D annotations.

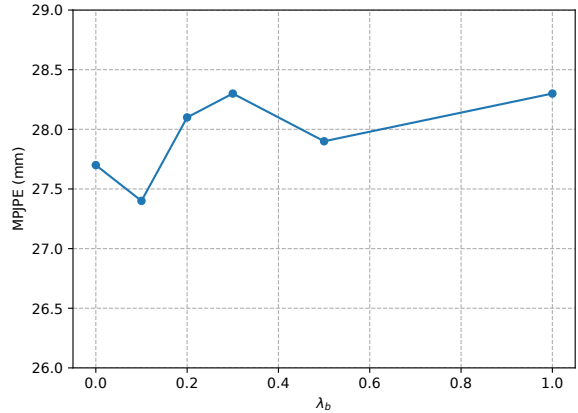


Figure 6: Evaluation of various weighting factors  $\lambda_b$  for bone direction consistency loss  $L_b$ . Experiments are conducted on Human3.6M with the MPJPE metric.

## 11 Robustness Evaluation

To evaluate the robustness of CV-UGCN, experiments are conducted on HumanEva-I dataset to test the tolerance for triangulation noises. To this end, we use 2D ground-truth poses for triangulation and train a single model following the train/test split in [Pavlo *et al.*, 2019; Lee *et al.*, 2018]. Then, triangulated poses added with the Gaussian noise of different variances are fed into the CV-UGCN for refinement. The results are shown in Table 7.

Although the 3D poses are triangulated from 2D ground truth, it

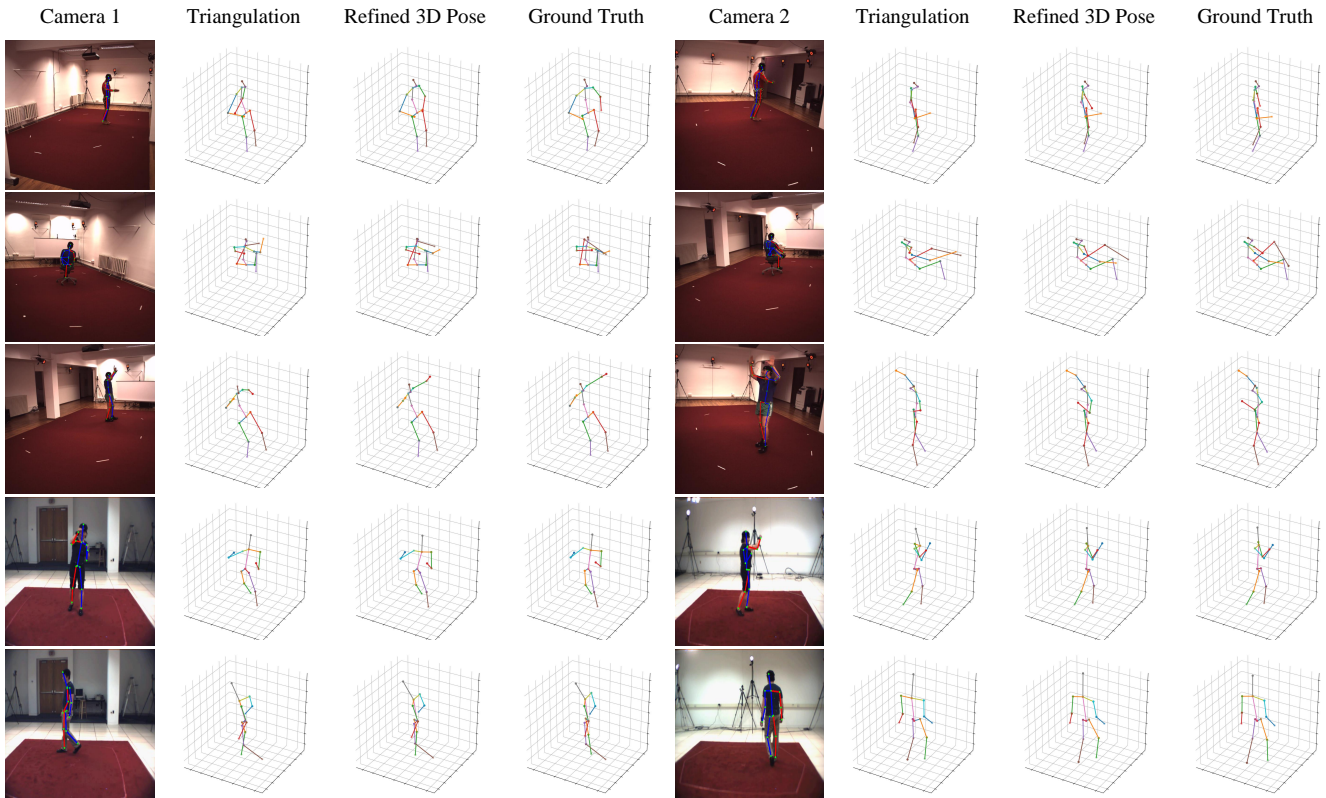


Figure 7: Qualitative results of our approach on the Human3.6M dataset (first 3 rows) and the HumanEva-I dataset (last 2 rows). The results of triangulation are noisy and unreliable, while our model is able to produce realistic and structurally plausible 3D poses.

still exists 6.0 mm P-MPJPE which maybe because of the camera calibration error. Our refinement model can refine the results to 3.0 mm, demonstrating the effectiveness of CV-UGCN. Besides, when the triangulated poses are added with Gaussian noises of different variances, the system seems not to be broken, with a stable improvement around 1.0 mm compared to the input coarse poses. It validates that our refinement model can perform reasonably and is robust to the coarse 3D poses with different levels of noise.

## 12 Visualization Results

More visualization results are given in Figure 7. Because of the error of 2D detections and camera calibration errors, the triangulation results are noisy and unreliable. Our refinement model can efficiently improve the coarse 3D poses to be more realistic and structurally plausible.

## 13 Applying to the Real Scene

We apply our method to the real scene to test the applicability. By using the stereo camera, we shoot a video in a room and use the proposed method to estimate the absolute 3D poses of the actor. Some visualization results are given in Figure 8.

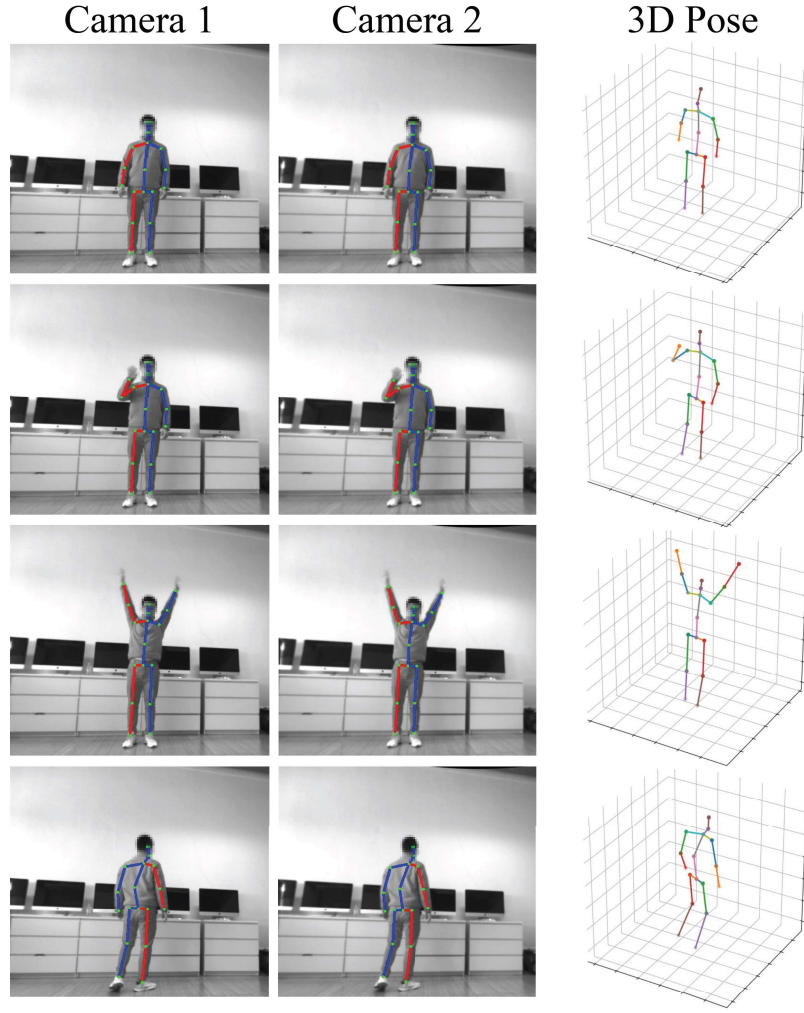


Figure 8: Visualization results of our method when applying to the real scene. Camera 1 and Camera 2 are the left and right views of a stereo camera.

Protocol #1	V	GT	Dir.	Disc	Eat	Greet	Phone	Photo	Pose	Purch.	Sit	SitD.	Smoke	Wait	WalkD.	Walk	WalkT.	Avg.
[Wandt and Rosenhahn, 2019]	1		77.5	85.2	82.7	93.8	93.9	101.0	82.9	102.6	100.5	125.8	88.0	84.8	72.6	78.8	79.0	89.9
[Tome <i>et al.</i> , 2017]	1		65.0	73.5	76.8	86.4	86.3	110.7	68.9	74.5	110.2	173.9	85.0	85.6	86.2	71.4	73.1	88.4
[Wang <i>et al.</i> , 2019]	1		-	-	-	-	-	-	-	-	-	-	-	-	-	-	-	86.4
[Martinez <i>et al.</i> , 2017]	1	✓	51.8	56.2	58.1	59.0	69.5	78.4	55.2	58.1	74.0	94.6	62.3	59.1	65.1	49.5	52.4	62.9
[Fang <i>et al.</i> , 2018]	1	✓	50.1	54.3	57.0	57.1	66.6	73.3	53.4	55.7	72.8	88.6	60.3	57.7	62.7	47.5	50.6	60.4
[Cai <i>et al.</i> , 2019]	1	✓	44.6	47.4	45.6	48.8	50.8	59.0	47.2	43.9	57.9	61.9	49.7	46.6	51.3	37.1	39.4	48.8
[Pavillo <i>et al.</i> , 2019]	1	✓	45.2	46.7	43.3	45.6	48.1	55.1	44.6	44.3	57.3	65.8	47.1	44.0	49.0	32.8	33.9	46.8
[Xu <i>et al.</i> , 2020]	1	✓	37.4	43.5	42.7	42.7	46.6	59.7	41.3	45.1	52.7	60.2	45.8	43.1	47.7	33.7	37.1	45.6
[Wang <i>et al.</i> , 2020]	1	✓	38.2	41.0	45.9	39.7	41.4	51.4	41.6	41.4	52.0	57.4	41.8	44.4	41.6	33.1	30.0	42.6
[Trumble <i>et al.</i> , 2017]	4	✓	92.7	85.9	72.3	93.2	86.2	101.2	75.1	78.0	83.5	94.8	85.8	82.0	114.6	94.9	79.7	87.3
[Kundu <i>et al.</i> , 2020]	4		-	-	-	-	-	-	-	-	-	-	-	-	-	-	-	85.8
[Iqbal <i>et al.</i> , 2020]	4		-	-	-	-	-	-	-	-	-	-	-	-	-	-	-	67.4
[Pavlakos <i>et al.</i> , 2017b]	4	✓	41.2	49.2	42.8	43.4	55.6	46.9	40.3	63.7	97.6	119.0	52.1	42.7	51.9	41.8	39.4	56.9
[Tome <i>et al.</i> , 2018]	4		43.3	49.6	42.0	48.8	51.1	64.3	40.3	43.3	66.0	95.2	50.2	52.2	51.1	43.9	45.3	52.8
[Chen <i>et al.</i> , 2019]	2		41.1	44.2	44.9	45.9	46.5	39.3	41.6	54.8	73.2	46.2	48.7	42.1	35.8	46.6	38.5	46.3
[Qiu <i>et al.</i> , 2019]	4		28.9	32.5	26.6	28.1	<b>28.3</b>	<b>29.3</b>	28.0	36.8	41.0	<b>30.5</b>	35.6	30.0	28.3	30.0	30.5	31.2
[He <i>et al.</i> , 2020]	4		29.0	<u>30.6</u>	27.4	<u>26.4</u>	31.0	31.8	26.4	<u>28.7</u>	<u>34.2</u>	42.6	32.4	<u>29.3</u>	<u>27.0</u>	<u>29.3</u>	<u>25.9</u>	30.4
[Remelli <i>et al.</i> , 2020]	4	✓	<u>27.3</u>	32.1	<b>25.0</b>	26.5	29.3	35.4	28.8	31.6	36.4	31.7	<u>31.2</u>	29.9	<b>26.9</b>	33.7	30.4	<u>30.2</u>
Ours	2		<b>25.6</b>	<b>27.7</b>	<u>25.3</u>	<b>24.5</b>	<u>29.1</u>	<u>29.5</u>	<b>23.5</b>	<b>25.7</b>	<b>31.2</b>	37.3	<b>28.9</b>	<b>24.9</b>	28.8	<b>24.6</b>	<b>24.8</b>	<b>27.4</b>

Table 5: Quantitative comparisons of Mean Per Joint Position Error (MPJPE) in millimeter on Human3.6M under protocol #1. GT means that the method uses 3D ground truth to train the model. V is the number of camera views for training and inference. The best score is marked in bold, second best is underlined.

Method	$P_1$	$P_2$	$P_3$	$P_4$	Avg.
triangulation	35.8	40.1	32.6	35.4	36.0
Training on $P_3$	<b>35.4</b>	<b>35.9</b>	26.5	<b>35.2</b>	33.3
Training on $P_1$ and $P_3$	28.2	<b>35.7</b>	25.9	<b>31.7</b>	30.4
Training on $P_2$ and $P_4$	<b>32.6</b>	30.7	<b>30.4</b>	27.1	30.2
Training on $P_1, P_2, P_3$	28.1	30.7	26.0	<b>31.1</b>	29.0
Training on $P_1, P_2, P_4$	27.9	30.9	<b>30.2</b>	27.2	29.1
Training on all pairs	27.4	30.3	25.3	26.8	27.4

Table 6: MPJPE Results (in mm) of our method on different camera paired views on Human3.6M. We evaluate the generalization capabilities of our approach testing on unseen camera paired views.  $P_i$  denotes  $i$ -th camera paired views. The results of the unseen paired views are marked in **bold**.

Train / Test	Triangulation	Refinement	$\Delta$
GT / GT	6.0	3.0	3.0
GT / GT + $\mathcal{N}(0, 5)$	8.5	6.7	1.2
GT / GT + $\mathcal{N}(0, 10)$	12.8	11.6	1.2
GT / GT + $\mathcal{N}(0, 15)$	17.6	16.7	1.1
GT / GT + $\mathcal{N}(0, 20)$	22.5	21.7	0.8

Table 7: Protocol #2 results on HumanEva-I dataset. The refinement model is trained with the triangulated 3D poses from 2D ground truth, and then tested on triangulated 3D poses added with Gaussian noises with different variances.